Ultramicroscopy 120 (2012) 10–15

Contents lists available at SciVerse ScienceDirect

Ultramicroscopy

journal homepage: www.elsevier.com/locate/ultramic

Nanohalos: A manifestation of electron channelling in gold nanoparticles

G. Ruben [a], P. Wang [b], A.J. D'Alfonso [a], P.D. Nellist [b], L.J. Allen [a,*]

[a] School of Physics, University of Melbourne, Parkville, Victoria 3010, Australia
[b] Department of Materials, University of Oxford, Oxford OX1 3PH, UK

ARTICLE INFO

Article history:
Received 27 March 2012
Received in revised form
30 May 2012
Accepted 4 June 2012
Available online 13 June 2012

Keywords:
Imaging gold nanoparticles
Scanning transmission electron microscopy (STEM)
Low-angle annular dark field (LAADF)

ABSTRACT

We discuss interesting haloing effects observed in experimental images of gold nanoparticles obtained using aberration-corrected scanning transmission electron microscopy (STEM) employing the low-angle annular dark-field (LAADF) imaging mode. The LAADF images contained bright rings of intensity (halos) with a diameter equal to or smaller than the diameter of the nanoparticle, the diameter varying as a function of the defocus of the STEM probe. Numerical simulations reveal that the halos are only present if the nanoparticles are imaged down a zone axis. Since the halos were observed in nearly all experimental images, this suggests that the nanoparticles become oriented along crystal zone axes during imaging.

© 2012 Elsevier B.V. All rights reserved.

1. Introduction

Scanning transmission electron microscopy (STEM) has been extensively used to image materials at atomic resolution, and in particular nanoparticles. The most widely used variant of STEM, Z-contrast imaging, is based on detecting electrons scattered to high angles after inelastic scattering during which a phonon is excited, a process also referred to as thermal diffuse scattering (TDS). Electron energy-loss spectroscopy (EELS) imaging has also been extensively developed [1]. Imaging using a low-angle annular dark-field (LAADF) detector is another possible mode of imaging which can potentially be used to detect buried layers [2].

The experimental geometry for STEM LAADF imaging is illustrated in Fig. 1(a). The LAADF imaging geometry employs a convergent electron probe with an annular detector in the diffraction plane whose inner aperture angle is only marginally greater than the probe forming aperture angle and hence is just outside the bright-field cone, similar to the proposal of Cowley and co-workers [3,4]. Electrons which have been scattered by the specimen, both elastically and inelastically (the latter mainly due to TDS) are then detected. It has recently been pointed out that this leads to enhancements in signal when the probe is on a column for probe defocus values Δf in the vicinity of interfaces, a phenomenon which is due to enhanced elastic scattering, TDS or a combination of both [2].

We have recently used the LAADF mode to image gold nanoparticles in the cytoplasm of a biological cell. The images were taken on the 200 kV Oxford-JEOL 2200MCO with third order spherical aberration correctors. Using a probe forming semi-angle of 24 mrad and with an annular detector aperture spanning a range of approximately 24–50 mrad, the images showed interesting bright rings (halos) of intensity when the probe was focussed away from the particles, as can be seen in Fig. 1(b). This is most evident in the topmost particle, where the periphery of the particle is clearly brighter than the centre. These halos disappear if the detector annulus is moved further away from the bright field cone, in other words for the medium angle annular dark-field (MAADF) imaging case (detector semi-angles approximately 30–64 mrad), as can be seen in Fig. 1(c). That image is qualitatively similar to that obtained by Z-contrast or high-angle annular dark-field (HAADF) imaging. Here we will explore the origin of the halos seen in the LAADF geometry and we show that they are essentially an electron channelling phenomenon. Furthermore, since the halos were observed in nearly all experimental images, this suggests that the nanoparticles become oriented along crystal zone axes during imaging.

2. Experiment and interpretation

To explore the occurrence of the halos shown in Fig. 1(b) we have obtained a focal series of STEM LAADF images using similar gold nanoparticles but now on the surface of an amorphous carbon film rather than in the cell. This provides a more controlled environment in which to explore this phenomenon since a given defocus of the STEM probe will be similar for all the particles being examined. The probe forming aperture was 19.5 mrad and the detector range was 21–34.7 mrad. Once again,

* Corresponding author. Tel.: +61 3 8344 7402; fax: +61 3 9347 4783.
E-mail address: lja@unimelb.edu.au (L.J. Allen).

0304-3991/$ - see front matter © 2012 Elsevier B.V. All rights reserved.
http://dx.doi.org/10.1016/j.ultramic.2012.06.002

halos were seen for almost all the particles with the size of the halo depending on the amount of defocus. The halo emerges from the centre of the image for large defocus (either under or over focus) values and becomes larger in diameter as the in focus condition is approached, eventually coinciding with the boundary of the particle profile at this focal position. The halo is less evident with the probe focussed within the particle. Halos on a number of nanoparticles can be seen in Fig. 2(a) and the corresponding (atomic resolution) images with the probe focussed near the top surfaces of the nanoparticles are shown in Fig. 2(b). Examination of Fig. 2(b) reveals that most of the nanoparticles are twinned, some exhibiting faceting. Recently Xu et al. [5] studied particles of similar size and shape to those discussed in this paper, which have diameters in the range of 10–20 nm. Such nanoparticles may exhibit a range of structures: decahedral, Ino decahedral, Marks' decahedral, truncated octahedral, and variations thereof [6,7]. High mobility of surface atoms, enhanced by energy from the focused electron probe, serves to round these particles, resulting in essentially two types of spheroidal particles; an fcc monocrystalline particle and a polycrystalline particle with typically five strained fcc segments joined at twinning planes. In particular, Xu et al. [5] studied the crystal structure of Marks'-decahedral gold nanoparticles of 20 nm mean diameter and found that the central axis lay along the [110] zone axis, consistent with our own observations.

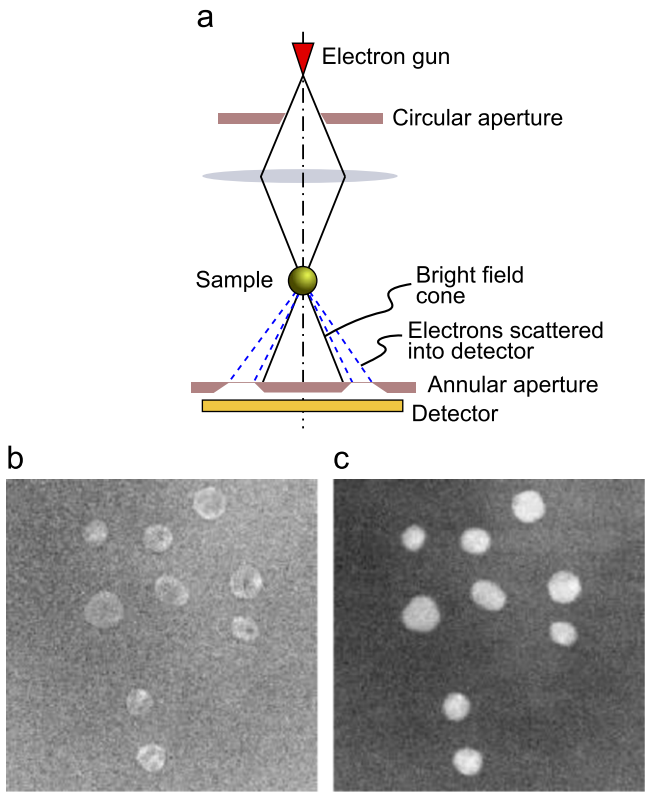

Fig. 1. (a) The LAADF geometry. (b) LAADF STEM image of gold nanoparticles within a biological cell showing the presence of bright rings (halos). (c) MAADF STEM images of the same nanoparticles.

However, some of the nanoparticles were observed to be monocrystalline and in Fig. 3(a)–(e) we show more detailed LAADF images of such a nanoparticle taken at the defocus values indicated. Defocus is defined relative to the centre of the nanoparticle with positive values corresponding to overfocus and negative values to underfocus. This case provides a good starting point for our modelling of the halo effect. We will return to multiply twinned nanoparticles later. The "in focus" image of the nanoparticle in Fig. 3(c) suggests that it is appropriate to approximate it by the spherically truncated monocrystalline structure shown in Fig. 4(a). We have carried out simulations which demonstrate that these halos rely on an electron channelling effect and, as we will show later, disappear if the particle is orientated away from a zone axis. Therefore the presence of the halos implies that the gold nanoparticles are oriented along a zone axis with respect to the beam during imaging. We consider propagation of the probe wave function through the specimen using the multislice absorptive model [8]. In this context the absorptive model gives results similar to the many-body quantum-mechanical model of [9] based on a Born–Oppenheimer approximation and which, in turn, yields numerically equivalent results to the well-known semi-classical frozen phonon (FPh) model [10,11].

The simulations in Fig. 3(f)–(j) show the same features as seen in the experimental data. The simulations were done assuming a diameter for the nanoparticle of 13.4 nm. The characteristic halos are particularly clear when line scans are extracted by averaging over a horizontal strip of pixels approximately 1.5 nm wide and symmetrically placed with respect to the centre of the particle, as shown in Fig. 3(k)–(o). We will now discuss the existence of halos and their size as a function of defocus. Our arguments will be based on Fig. 5, which schematically shows the STEM probe relative to the particle for a range of defocus values. Inspection of this figure shows that as the defocus of the probe varies across

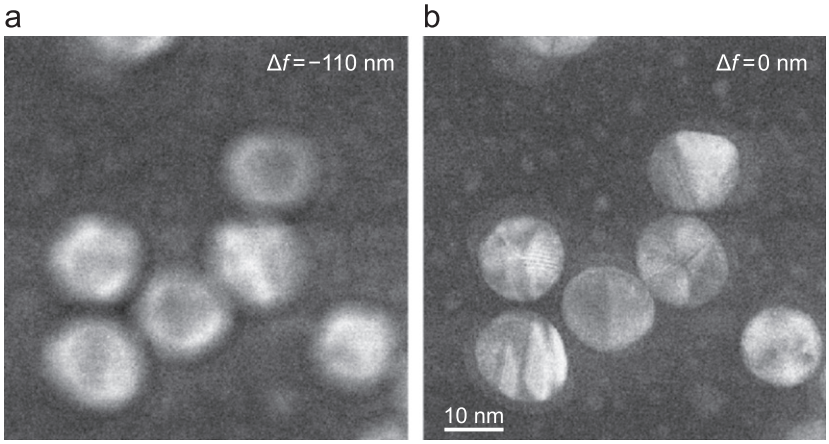

Fig. 2. LAADF STEM images of polycrystalline gold nanoparticles on an amorphous carbon film. (a) Images at an underfocus $\Delta f = -110$ nm showing the presence of halos. (b) In focus images of the same particles ($\Delta f \approx 0$ nm) show atomic columns and structure due to internal twinning planes is discernible.

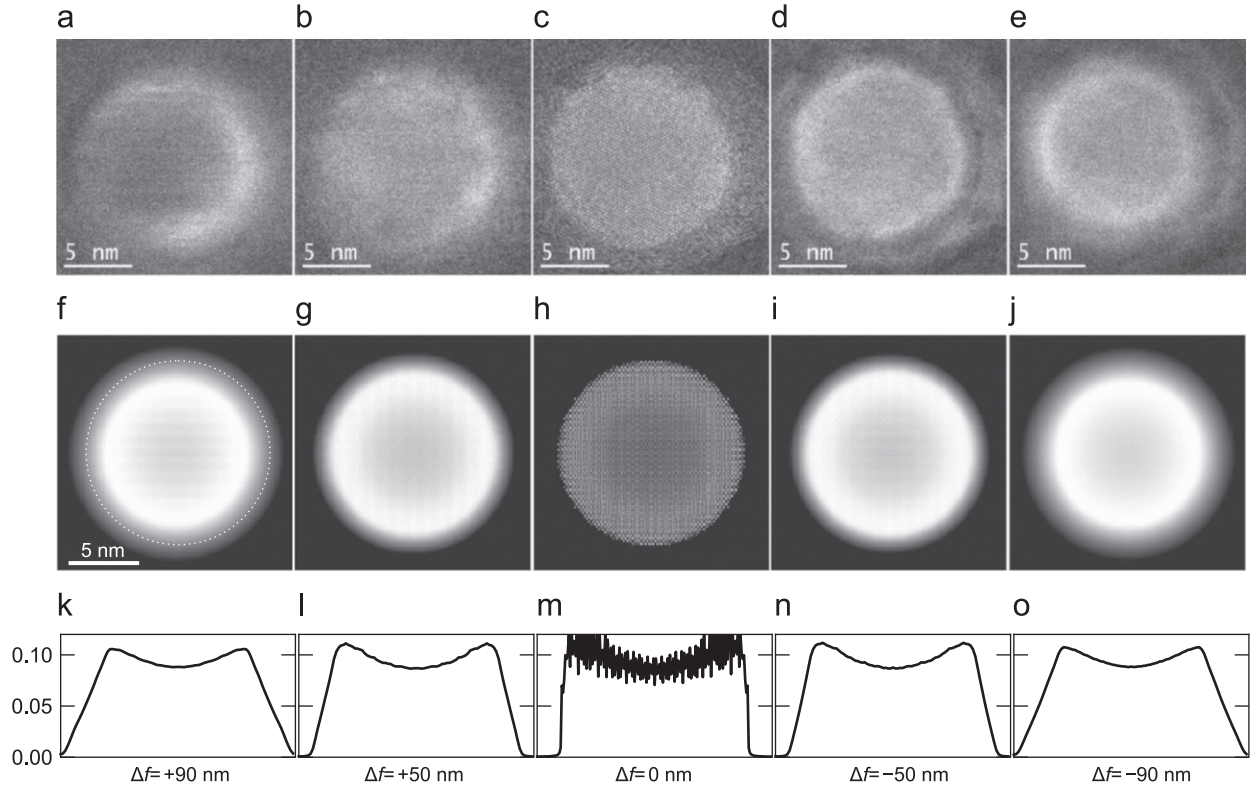

Fig. 3. Experimental (a)–(e) and simulated (f)–(j) LAADF STEM images of a monocrystalline gold nanoparticle for the defocus values Δf indicated. In (k)–(o) we show line plots extracted from the corresponding simulations (directly above in each case) as described in the text. The common scale ranging from 0.0 to 0.1 is the fractional intensity into the detector relative to the incident flux of electrons.

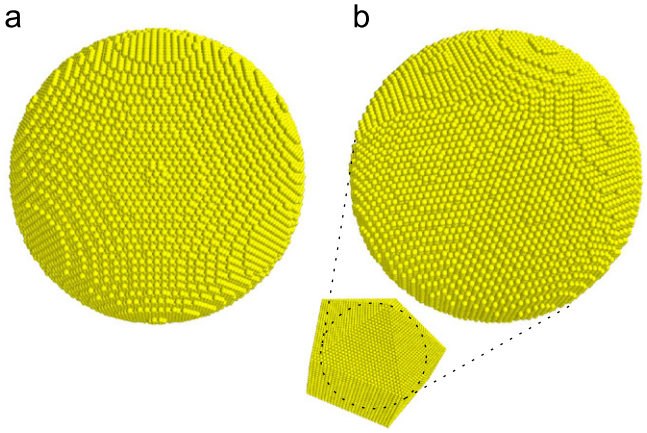

Fig. 4. Models of gold nanoparticles. (a) The fcc structure truncated to a sphere. (b) Decahedral structure truncated to a sphere. The inset shows an Ino decahedral structure from which a spherical region shown in (b) has been extracted.

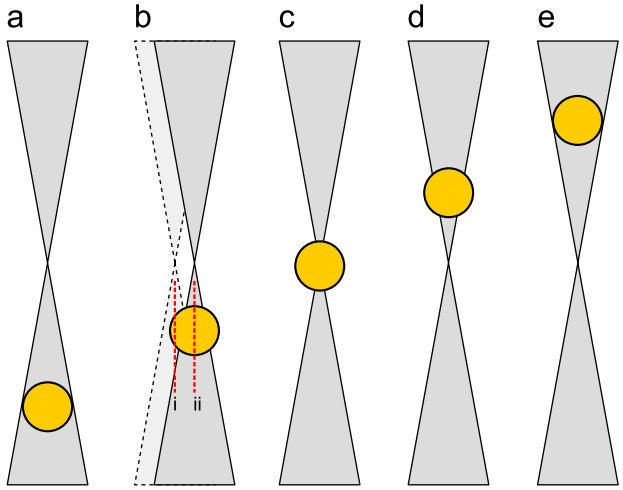

Fig. 5. Schematic showing the change in geometry of the probe–nanoparticle interaction from (a) maximum overfocus to (e) maximum underfocus. The dotted lines in (b) refer to the probe positions in Fig. 6. (For interpretation of the references to colour in this figure, the reader is referred to the web version of this article.)

the range shown, two pertinent things happen. Firstly the interaction volume of the probe with the particle changes, becoming smaller for defocus values closer to zero for all transverse probe positions. Secondly the intensity of the probe in the interaction volume increases as the defocus becomes closer to zero and consequently the coupling to the atomic columns in the particle also increases [12].

For very large overfocus the illumination across the particle is approximately planar. Let us now reduce the amount of defocus to that shown in Fig. 5(a), where the probe is overfocussed in such a way that the bright field cone just encompasses the particle when the probe is symmetrically placed with respect to the approximately spherical nanoparticle. Then sweeping the probe across the particle from the left, the signal rises as the interaction volume increases and reaches a maximum when the particle is centrally aligned. The signal then reduces to a minimum again as the probe moves off the particle. However, this purely geometric effect is attenuated by channelling, which has the effect of drawing electrons onto the atomic columns, focussing them towards the forward direction and hence inside the inner angle of the LAADF detector. In the symmetric illumination condition, where the coupling of the probe to the atomic columns in the particle is a maximum, the reduction in signal due to channelling is sufficiently small that one still obtains the maximum signal for this probe position and no halo is observed.

Let us now consider the situation shown in Fig. 5(b), an overfocus intermediate between that in Fig. 5(a) and the in focus situation shown in Fig. 5(c). In this case the signal into the LAADF detector is rising, due to increasing interaction volume, as the probe moves from the left. The whole probe now illuminates the particle before the symmetric position is reached and the illumination is also more intense. Once this strong coupling is established, channelling reduces the signal into the LAADF detector sufficiently to reduce the signal relative to previous probe positions and a halo develops. Furthermore, higher thickness leads to enhanced channelling, reducing the intensity scattered to the LAADF detector as discussed in more detail in the next paragraph. This thickness effect is clearly evident at focus in Fig. 3(h).

To provide insight into the role of channelling we calculate azimuthally summed scattering distributions in Fig. 6. These are obtained by Fourier transforming the probe wave function in real space at each depth and then summing the intensity radially over the range of 0–40 mrad. The intensity outside a polar angle corresponding to that defined by the bright field cone (19.5 mrad in this case) is a measure of the signal into the LAADF detector for the depth corresponding to the exit surface. We consider the two probe positions schematically indicated in Fig. 5(b) by the vertical red lines. In Fig. 6(a) we show the results for an overfocus $\Delta f = 90$ nm and for a probe position where the path length through the particle is half the radius, indicated by position i in Fig. 5(b) (assuming a simple geometrical model for the probe radius taking into account the maximum convergence angle). The two white lines indicate where the axis of the probe intersects the top and bottom surfaces of the nanoparticle. We see from the flux at polar angles greater than 19.5 mrad that scattering into the LAADF detector increases along the probe axis and is maintained towards the exit surface. On the other hand when the probe is symmetrically placed in the position indicated by ii in Fig. 5(b), the result in Fig. 6(b) shows that soon after the strongly coupling probe enters the nanoparticle (at depth 0 nm) there is considerable scattering that, if the particle were to truncate at around 5 nm, would lead to a strong LAADF signal. However, the subsequent channelling up to the exit surface (indicated by the white line at 13.6 nm) shows clearly that electrons once destined for the LAADF detector are instead pulled back towards polar angles inside the bright field cone and hence are not detected. This channelling is the mechanism by which the halos are generated. To underline this, calculations are shown in Fig. 6(c) and (d) which correspond to Fig. 6(a) and (b) in all respects excepting that they are for a non-channelling condition. In that case electron flux is not drawn back inside the inner-angle of the bright field detector.

Let us return now to Fig. 5, in particular part (c). When the probe is focussed in the vicinity of the nanoparticle the signal initially rises as the probe sweeps onto the particle and, due to the small area of the nanoparticle on which the probe is focussed, strong coupling to columns of atoms with the concomitant channelling is rapidly established. We then see lattice resolution imaging of the columns as the probe sweeps across the particle. The halo now has its maximum diameter and is not very prominent. When focussing below the particle, i.e. for underfocus, as shown in Fig. 5(d) we have a similar situation to the discussion of Fig. 5(b), except that the channelling conditions are not the same—in this case the probe is converging rather than diverging. This leads to the subtle variations in the images for the same underfocus and overfocus values, as can be seen in Fig. 3. However, there is an approximate symmetry between the overfocus and underfocus scenarios, since the effect of channelling in each case is to focus electrons towards the centre of the bright field disc. Lastly in Fig. 5(e) we show the case where the underfocussed probe just encapsulates the particle geometrically and, as for the case in Fig. 5(a), no halo is observed. (Both these cases are outside the range of defocus values shown in Fig. 3.)

In Fig. 7 the relationship between defocus and the distance D from the edge of the nanoparticle to the halo, as indicated in the figure, is plotted for the experimental defocus series from which

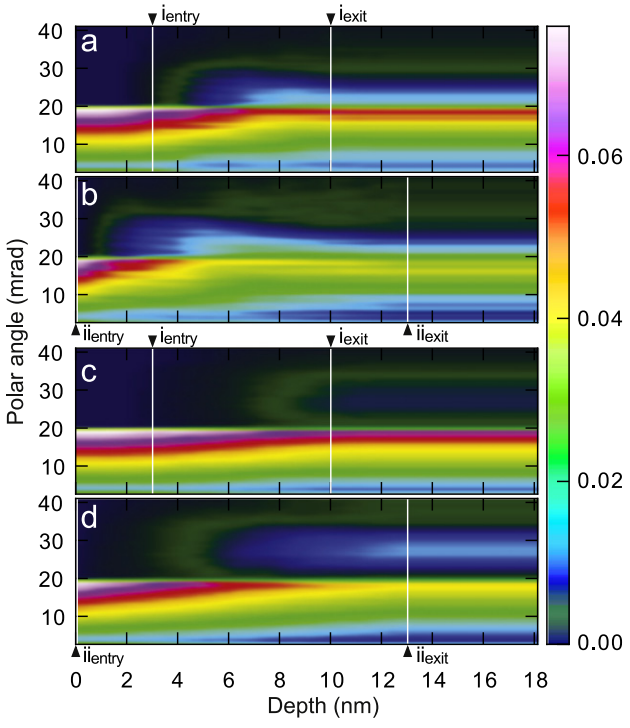

Fig. 6. Azimuthally summed scattering distributions in reciprocal space for a single defocus of +90 nm [cf. Fig. 3(f)] for the probe aligned on the ⟨110⟩ zone axis and positioned symmetrically along (a) the line labelled i in Fig. 5(b) and in (b) along the line labelled ii in Fig. 5(b). White lines indicate the entrance and exit surfaces of the nanoparticle for the probe positions i and ii. In (c) and (d) we have the corresponding calculations to (a) and (b) but the probe is now not down a zone axis. The zero on the depth scale corresponds to the highest point on the entrance surface of the nanoparticle.

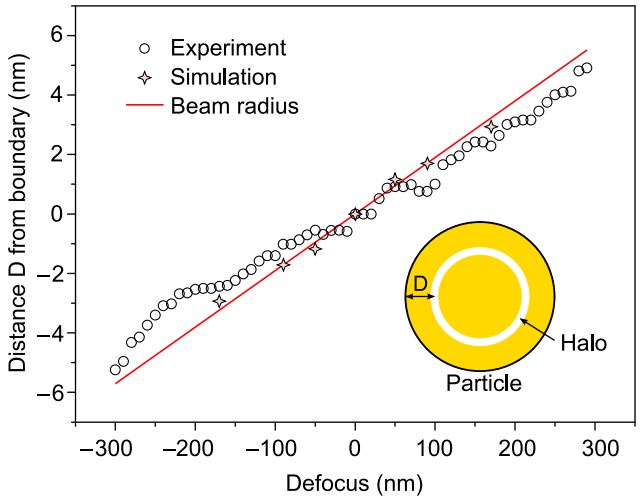

Fig. 7. The relationship between defocus and the distance D from the edge of the nanoparticle to the halo is plotted for the experimental defocus series from which the results in Fig. 3 were extracted. The distance D has been taken to be negative for underfocus. This is compared with the beam radius at the particle in each case, once again using a similar sign convention. The calculated distances D from the simulations in Fig. 3(f)–(j) plus two further defocus values (± 170 nm) are also indicated.

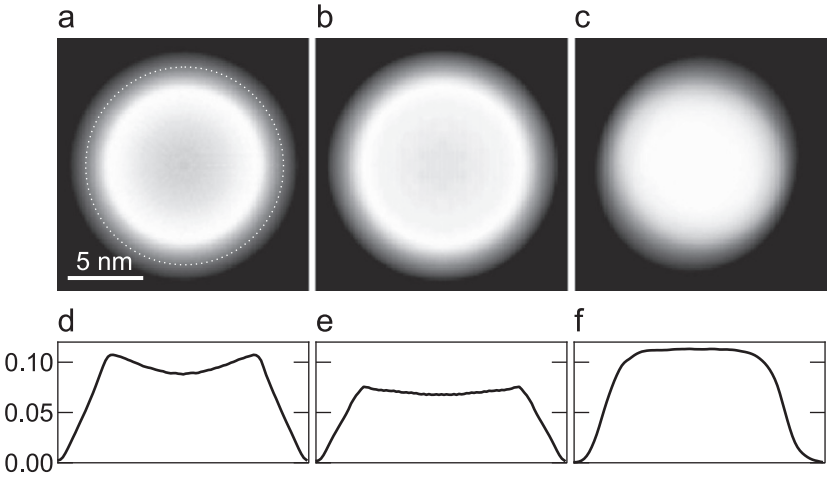

Fig. 8. LAADF STEM images for (a) an fcc monocrystalline specimen down the ⟨111⟩ zone axis, (b) a polycrystalline spherically truncated decahedral particle with ⟨110⟩ zone axes in common and (c) a similar sized nanoparticle not aligned with a zone axis. The defocus value in each case is $\Delta f = -90$ nm. In (d)–(f) we show line plots extracted from the corresponding simulations (directly above in each case), as was done in Fig. 3. In (d)–(f) the common scale ranging from 0.0 to 0.1 is the fractional intensity into the detector relative to the incident flux of electrons.

the results in Fig. 3 were extracted. The distance D has been taken to be negative for underfocus. This is compared with the beam radius at the particle in each case, once again using a similar sign convention. This shows a close to linear relationship and furthermore simulated results are in close agreement with what is found experimentally. Fig. 7 clearly demonstrates that the maximum intensity (i.e. the halo position) occurs when the projected overlap between the probe and the particle just achieves its maximum value, resulting in a value of D that matches the probe radius.

We have done calculations for other zone axes and the haloing effect is maintained. A result which is representative of these calculations is shown in Fig. 8(a), which is for the ⟨111⟩ zone axis for a defocus $\Delta f = -90$ nm. The halo is clearly evident from inspection of the extracted line scan in Fig. 8(d). We have also done a simulation, for the same defocus, using a spherically truncated decahedral particle model which approximates the twinned structures observed, some of which are shown in Fig. 2. Here the individual segments are aligned with the probe along the ⟨110⟩ zone axis. The resulting LAADF STEM image is shown in Fig. 8(b) with the corresponding line scan in Fig. 8(e). The intensity contains the halo as expected, along with subtle additional five-fold symmetric fringes due to the twinning planes. For all the calculations discussed so far, the model has been aligned along a major zone axis. However, calculations away from a zone axis do not show the halo structure. A typical result of such an off zone axis (and therefore non-channelling) orientation is shown in Fig. 8(c), also calculated for a defocus of $\Delta f = -90$ nm. The corresponding line scan in Fig. 8(f) confirms that there is no halo. This shows that the results in Fig. 7 should not be interpreted in a simple geometric way but that channelling underlies the formation of the halos.

It is noted that the images of nanoparticles within the biological cell or placed on a carbon substrate generally exhibited a halo structure. This is particularly significant as we have observed that the halos are only present in simulations if the nanoparticles are aligned along a zone axis. We therefore conclude that in the two experiments reported here the nanoparticles are aligned with zone axes parallel to the optical axis and this alignment was found experimentally to be along the [110] zone axis. Mechanisms behind this alignment are beyond the scope of this work and remain a topic of further investigation. One possible mechanism could be the so-called "electron wind" caused by the momentum and energy transfer to the specimen by the probing fast electron [13]. Recent evidence for this mechanism has recently been observed in the bulk motion and rotation of smaller gold nanoparticles [14]. Alternatively it has also been pointed out that, due to the high charge mobility of gold nanoparticles, an induced dipole moment is created in the presence of an external electric field [15–17]. It is conceivable that the torque associated with this dipole moment could be of a sufficient magnitude to cause a rotation of the particle with respect to the local environment.

3. Conclusions

Haloing effects were observed in images of gold nanoparticles obtained in the LAADF imaging mode. The LAADF images contained bright rings of intensity (halos) varying in a linear way as a function of the defocus of the STEM probe. Numerical simulations reveal that the halos are due to channelling of the probe electrons in the nanoparticles. The results in Fig. 7 show that it is possible to use the relationship between halo diameter and defocus to determine the z-location of nanoparticles relative to each other.

Acknowledgements

P.W. and P.D.N. acknowledge financial support by the EPSRC (EP/F048009/1). This research was supported under the Discovery Projects funding scheme of the Australian Research Council (Project DP110102228).

References

[1] S.J. Pennycook, P.D. Nellist (Eds.), Scanning Transmission Electron Microscopy, Springer, New York, 2011.
[2] G. Ruben, E.C. Cosgriff, A.J. D'Alfonso, S.D. Findlay, J.M. LeBeau, L.J. Allen, Interface location by depth sectioning using a low-angle annular dark field detector, Ultramicroscopy 113 (2012) 130–131.
[3] J. Cowley, M. Hansen, S.-Y. Wang, Imaging modes with an annular detector in STEM, Ultramicroscopy 58 (1995) 18–24.
[4] M. Cowley, STEM imaging with a thin annular detector, Journal of Electron Microscopy (Tokyo) 50 (2001) 147–155.
[5] X.J. Xu, Z. Saghi, B.J. Inkson, G. Möbus, Three-dimensional characterization of multiply twinned nanoparticles by high-angle tilt series of lattice images and tomography, Journal of Nanoparticle Research 12 (2010) 1045–1053.
[6] A.S. Barnard, N. Young, A.I. Kirkland, M.A. van Huis, H. Xu, Nanogold: a quantitative phase map, ACS Nano 3 (2009) 1431–1436.
[7] A.S. Barnard, Modelling of nanoparticles: approaches to morphology and evolution, Reports on Progress in Physics 73 (2010) 086502.

[8] L.J. Allen, S.D. Findlay, M.P. Oxley, C.J. Rossouw, Lattice-resolution contrast from a focused coherent electron probe. Part I, Ultramicroscopy 96 (2003) 47–63.
[9] B.D. Forbes, A.V. Martin, S.D. Findlay, A.J. D'Alfonso, L.J. Allen, Quantum mechanical model for phonon excitation in electron diffraction and imaging using a Born–Oppenheimer approximation, Physical Review B 82 (2010) 104103.
[10] R.F. Loane, P. Xu, J. Silcox, Thermal vibrations in convergent-beam electron diffraction, Acta Crystallographica A 47 (1991) 267–278.
[11] S. Hillyard, R.F. Loane, J. Silcox, Annular dark-field imaging: resolution and thickness effects, Ultramicroscopy 49 (1993) 14–25.
[12] A.J. D'Alfonso, S.D. Findlay, M.P. Oxley, S.J. Pennycook, K. van Benthem, L.J. Allen, Depth sectioning in transmission electron microscopy based on core-loss spectroscopy, Ultramicroscopy 108 (2007) 17–28.
[13] L.D. Marks, J.P. Zhang, Is there an electron wind? Ultramicroscopy 41 (1992) 419–422.
[14] P.E. Batson, A. Reyes-Coronado, R.G. Barrera, A. Rivacoba, P.M. Echenique, J. Aizpurua, Plasmonic nanobilliards: controlling nanoparticle movement using forces induced by swift electrons, Nano Letters 11 (2011) 3388–3393.
[15] N.G. Green, T.B. Jones, Numerical determination of the effective moments of non-spherical particles, Journal of Physics D: Applied Physics 40 (2007) 78–85.
[16] J. Park, W. Lu, Orientation of core–shell nanoparticles in an electric field, Applied Physics Letters 91 (2007) 053113.
[17] C.D. Daub, D. Bratko, T. Ali, A. Luzar, Microscopic dynamics of the orientation of a hydrated nanoparticle in an electric field, Physical Review Letters 103 (2009) 207801.